Elsevier Editorial System(tm) for Remote Sensing of Environment
Manuscript Draft

Manuscript Number:

Title: Automatic Bedrock and Ice Layer Boundaries Estimation in Radar Imagery Based on Level Set Approach

Article Type: Research Paper

Keywords: Radar Imagery
Bedrock and ice layers
Levelset

Corresponding Author: Dr. Maryam Rahnemoonfar,

Corresponding Author's Institution: Texas A&M University-Corpus Christi

First Author: Maryam Rahnemoonfar

Order of Authors: Maryam Rahnemoonfar; Geoffrey Fox; Masoud Yari

***Highlights (for review)**

Research Highlights:

- Developing an automatic technique to detect bedrock and ice layers boundary
- Complex topology of ice and bedrock boundary layers can be detected
- The results are evaluated on airborne radar imagery over Antarctica and Greenland
- Achieving very high accuracy in respect to hand-labeled ground truth

Automatic Bedrock and Ice Layer Boundaries Estimation in Radar Imagery Based on Level Set Approach

Maryam Rahnemoonfar[1], Geoffrey C. Fox[2], Masoud Yari[3]

1 Department of Computing Sciences, Texas A&M University-Corpus Christi, TX 78412
2 School of Informatics and Computing, Indiana University, Bloomington
3 Department of Engineering, Texas A&M University-Corpus Christi, TX 78412

Abstract

Accelerated loss of ice from Greenland and Antarctica has been observed in recent decades. The melting of polar ice sheets and mountain glaciers has a considerable influence on sea level rise in a changing climate. Ice thickness is a key factor in making predictions about the future of massive ice reservoirs. The ice thickness can be estimated by calculating the exact location of the ice surface and hidden bedrock beneath the ice in radar imagery. Identifying ice surface and bedrock locations is typically performed manually which is a very time consuming procedure. Here we propose an approach which automatically detects ice surface and bedrock boundaries using distance regularized level set evolution. In this approach the complex topology of ice and bedrock boundary layers can be detected simultaneously by evolving an initial curve in radar imagery. Using a distance regularized term, the regularity of the level set function is intrinsically maintained that solves the reinitialization issues arising from conventional level set approaches. The results are evaluated on a large dataset of airborne radar imagery collected during IceBridge mission over Antarctica and Greenland and show promising results in respect to hand-labeled ground truth.

1. Introduction

In recent years global warming has caused serious damages to our environment. Accelerated loss of ice from Greenland and Antarctica has been observed in recent decades. The melting of polar ice sheets and mountain glaciers has a considerable influence on sea level rise and altering ocean currents, potentially leading to the flooding of the coastal regions and putting millions of people around the world at risk. Therefore precise calculation of ice thickness is very important for sea level rise and flood monitoring. Moreover the shape of bedrock hidden beneath the thick ice sheets is a key factor in predicting the ice motion and the future locations of massive ice reservoirs and their contribution to sea level rise in changing climates. The hidden terrain beneath the thick ice has fascinated researchers for many years. Radar sensor is the only instrument that can penetrate through ice and give information about the hidden bedrock beneath layers of ice. The multichannel coherent Radar depth sounder was used during IceBridge mission (Allen et al., 2012) to provide important information about polar ice thickness and its changes during time. Ice thickness can be determined by distinguishing layers of different dielectric constants such as air, ice, and rock in radar echograms. Figure 1 shows a sample image produced by radar echogram. The horizontal axis is along flight path and the vertical access represents depth. The dark line on the top of the image is the boundary between air and ice while the more irregular lower boundary represents the bedrock which is the boundary between ice and the terrain. The bedrock hidden beneath the thick ice sheets can take any shape from smooth to mountainous (figure 1).

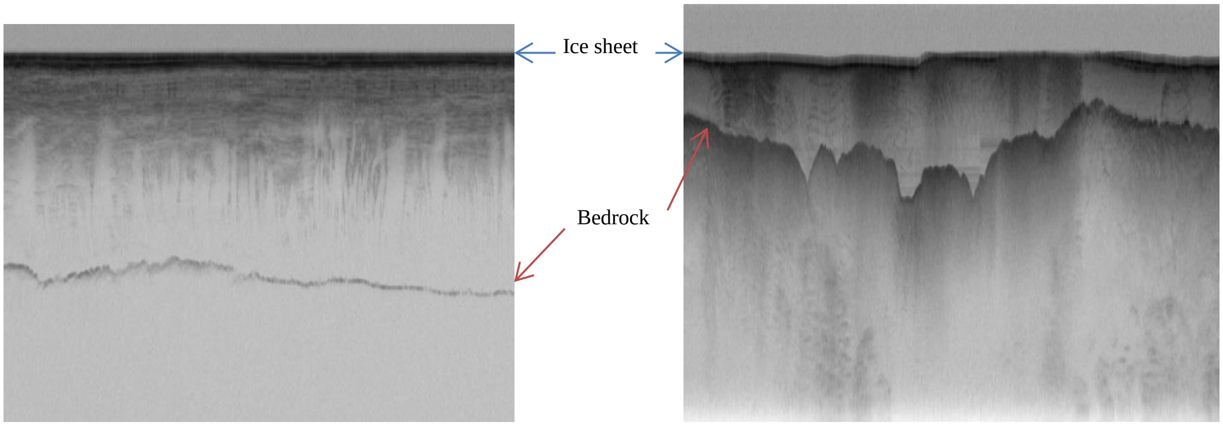

Figure 1: Ice sheet and bedrock depicted in radar echogram gathered by the Multichannel Coherent Radar Depth Sounder

The large variability of bedrocks shape along with speckle noise inherits from the coherent nature of SAR images, make the identification and interpretation of bedrocks quite difficult. Usually human experts mark ice sheet layer and bedrock by hand for further processing. Manual layer identification is very time consuming and is not practical for regular, long-term ice-sheet monitoring. The development of automated techniques is thus fundamental for proper data management.

This paper proposes a novel level set approach to automatically identify ice layer and bedrock in a large dataset of radar imagery. In this approach the image will be segmented by an initial curve into two parts: inside the curve (negative interior) and outside the curve (positive exterior). At the next step, each point on the curve will move at variable speeds depending on their distance from the center of the curve. Nearer points move faster while further points move at lower speeds. In the case of having a feature in the image, shrinking (expanding) curve will stop at the boundary of the shape. This process will continue until all boundaries are detected. In conventional level set formulation, the level set function typically develops irregularities during its evolution and needs re-initialization to periodically replace the degraded level-set function. Here we used a variational level set function in which the regularity of level set function is maintained intrinsically.

After this introduction, the related works will be discussed in section 2. The details of the proposed method will be discussed in section 3. Experimental results will be discussed in section 4. Finally conclusions are drawn in section 5.

2. Related works

Several semi-automated and automated methods have been introduced in the literature for layer finding and ice thickness in radar images (Crandall et al., 2012; Fahnestock et al., 2001; Ferro and Bruzzone, 2011; Freeman et al., 2010; Frigui et al., 1900; Gifford et al., 2010; Ilisei et al., 2012; Karlsson et al., 2013; Lee et al., 2014; Mitchell et al., 2013a; Mitchell et al., 2013b; Sime et al., 2011). Freeman et al. (Freeman et al., 2010) find near surface ice layers in images form the shallow subsurface radar on NASA's Mars reconnaissance Orbiter (SHARAD). First the layers were transformed to horizontal layers and then several filtering and thresholding techniques were applied to enhance the image and discard unclear layers. Finally the layers were transformed back to image space. Our algorithm is quite distinct from this method in a sense that it does not need any intermediate thresholding which might be different from one image to another. Ferro & Bruzzone (Ferro and Bruzzone, 2011) proposed an algorithm to extract the deepest scattering area visible in radargrams of SHARAD mission acquired on the north polar Layered Deposits of Mars. Their algorithm is based on the statistical properties of subsurface targets and finding a suitable fitting model. This method is unable to find exact layers of ice sheet and only find an approximate location of different sub-regions merely based on the statistical analysis of the signal.

Several works in the literature use graphical models to detect land mine (Frigui et al., 1900) or ice layers (Crandall et al., 2012) (Lee et al., 2014) in radar echograms. Frigui *et al* (Frigui et al., 1900) proposed a system for land mine detection using ground-penetrating radar. Their proposed system includes a hidden Markov model based detector, a corrective training component, and an incremental update of the background model. Crandall et al (Crandall et al., 2012) used probabilistic graphical models for detecting ice layer boundary in echogram images. Their model incorporates several types of evidence and constraints including that layer boundaries should lie along areas of high image contrast and that layer boundaries should be continuous and not intersect. The extension of this work was presented in (Lee et al., 2014) where they used Markov-Chain Monte Carlo to sample from the joint distribution over all possible layers conditioned on an image. Gibbs sampling instead of dynamic programming based solver was used for performing inference. The problem with using graphical models is that it needs a lot of training samples (around half of the actual dataset) which are ground-truth images labeled manually by human. Given the fact that manual ice layer detection is a very time consuming and expensive task, the last three methods are not practical for large dataset.

In another work, Gifford *et al* (Gifford et al., 2010) compared the performance of two methods, edge based and active contour, for automating the task of estimating polar ice and bedrock layers from airborne radar data acquired over Greenland and Antarctica. They showed that edge-based approach offers faster processing but suffers from lack of continuity and smoothness aspects that active contour provides. In active contour approach, the contour's shape is adaptively modified and evaluated to minimize cost or energy in the image (Chan and Vese, 2001; Kass et al., 1988). The main disadvantage of the active contour model is the incapability of maintaining the topology of evolving curve. This difficulty does not arise in the level set model as it embeds the evolving curve into a higher dimensional surface. Mitchell et al (Mitchell et al., 2013b) used level set technique for estimating bedrock and surface layers. However for each single image the user needs to re-initialize the curve manually and as a result the method is quite slow and was applied only to a small dataset. In this paper, the regularity of level set is intrinsically maintained using a distance regularization term. Therefore it does not need any manual re-initialization and was automatically applied on a large dataset.

3. Methodology

Here we propose to use level sets technique to precisely detect ice layer and bedrock boundary. The level set method (LSM) is essentially a successor to the active contour method. Active contour method (ACM), also known as Snake Model, was first introduced by Kass *et al* (Kass et al., 1988). The ACM is designed to detect interfaces and boundaries by a set of parametrized curves (contours) that march successively toward the desired object until the desired interfaces are captured. We present the parametrized curves as

$$C(s,t)=(x(s,t),y(s,t)), \quad s\in[0,1], \quad t\in[0,\infty) \tag{1}$$

where s is the parameter of the curve length and t is the temporal variable. The idea is that the curve $C(s,t)$ approaches to the desired object as time increases until it captures the desired interface. The motion of the curves is due to the influence of a vector field created based on properties of the desired feature in image, so that it can eventually lead the curve to the boundaries of the desired object.

Generally speaking, the curve $C(s,t)$ moves and eventually captures the interface of the desired object according to the following differential equation

$$\frac{\partial C}{\partial t} = FN \qquad (2)$$

where F is the velocity function for the moving curve *C* and *N* determines the direction of the motion. Here *N* is the normal vector to the curve C.

The ACM is an efficient tool in image and video segmentation, but it suffers from certain serious issues. As mentioned before, the main disadvantage of the ACM is that it is incapable to maintain the topology of the evolving curve; therefore, it can introduce misleading complexities in the process. To overcome the disadvantages that the snakes model presents, the level set method (LSM) was proposed by Osher and Sethian (Osher and Sethian, 1988). Rather than following the interface itself as in ACM, the level set method takes the original curve and builds it into a surface. In other words, the LSM takes the problem to one degree higher in spatial dimension (Figure 2) and considers the curve $C(s,t)$ as the zero-level of a surface $z = \varphi(x,y,t)$ at any given time t. The function φ is called the level set function (LSF).

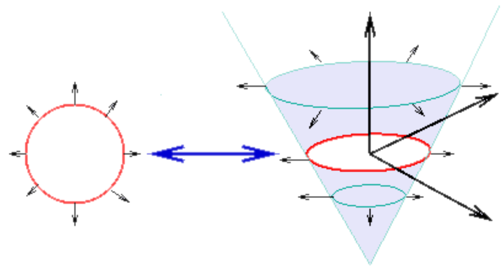

Figure 2: Level Set Method

Suppose the curve $C(s,t)$ is the interface of an open region $\Omega_t \subset \mathbb{R}^2$. We embed the curve $C(s,t)$ in the surface $z=\varphi(x,y,t)$ in a way that the curve $C(s,t)$ will be the zero level set while LSF, φ, takes negative values inside C and positive values outside of it. That is

$$\varphi(x,t)=0 \text{ for } x\in\partial\Omega_t, \tag{3}$$

and

$$\begin{aligned}\varphi(x,t)<0 \; for \; x\in\Omega_t,\\ \varphi(x,t)>0 \; for \; x\notin\bar{\Omega}_t.\end{aligned} \tag{4}$$

In this setting, the LSF, φ, is the solution of the following dynamical system

$$\frac{\partial\varphi}{\partial t}=-\frac{\partial\mathcal{F}}{\partial\varphi} \qquad (x,t)\in\Omega\times[0,\infty] \tag{5}$$

with a typical initial condition. Conventionally in image segmentation approaches the LSF functional $\mathcal{F}$ is defined as the sum of the edge force and the area force:

$$\mathcal{F}=\mathcal{E}_{edge}+\mathcal{E}_{area} \tag{6}$$

where

$$\mathcal{E}_{edge}(\varphi) = \lambda \int_{\Omega} g\delta(\varphi)|\nabla\varphi| dx \tag{7}$$

$$\mathcal{E}_{area}(\varphi) = \alpha \int_{\Omega} gH(-\varphi) dx \tag{8}$$

with α, λ a real constant and $\lambda > 0$. The functions δ and H are the Dirac and Heaviside functions respectively. The function g is the edge indicator on Ω, area of the image, which is defined by

$$g = \frac{1}{1 + |\nabla G_{\sigma} * I|^2} \tag{9}$$

where I is the image intensity and G_{σ} is a Gaussian Kernel with a standard deviation σ.

The edge term, $\mathcal{E}_{edge}$ computes the line integral along the zero level contour of φ; that is, $\int_0^1 g(C(s))|C'(s)|ds$, where the curve $C = C(s):[0,1] \to \Omega$ is the zero-level contour and s is the curve length. This term will be minimized when C is positioned on the boundary of the desired object. The area term, $\mathcal{E}_{area}$, is basically calculated as a weighted area of the region inside the zero level contour. It accelerates the motion of the zero-level contours toward the desired object.

Therefore, to minimize the energy functional $\mathcal{F}$, it is necessary to solve the following PDE system:

$$\begin{aligned} &\frac{\partial\varphi}{\partial t} = \lambda\delta(\varphi)\operatorname{div}\left(g\frac{\nabla\varphi}{|\nabla\varphi|}\right) + \alpha g\delta(\varphi) \qquad (x,t) \in \Omega\times[0,\infty) \\ &\varphi(x,0) = \varphi_0(x) \end{aligned} \tag{10}$$

For this system we consider the Neumann boundary condition on Ω, which signifies that there is no external force outside the image area. To carry out a numerical process to solve this PDE system, the spatial derivatives are discretized using the upwind scheme. The use of the central difference scheme will result in instability in the numerical procedure. The numerical procedure also involves the assumption that $|\nabla\varphi|=1$. We initialize the procedure with a function that satisfies this property, but the numerical scheme will not pass on this property; consequently at each step an extra care, known as re-initialization, must be taken to avoid the error accumulation. The reinitialization procedure involves solving the following PDE system for ψ in each step

$$\frac{\partial\psi}{\partial t} = sign(\varphi)(1-|\nabla\psi|) \tag{11}$$

This severely slows down the computation. To overcome this difficulty we use the distance regularization method proposed in (Li et al., 2005) (Li et al., 2010). In DSLR method, the LSF functional $\mathcal{F}$ is defined as

$$\mathcal{F} = \mathcal{E}_{edge} + \mathcal{E}_{area} + \mathcal{E}_p \tag{12}$$

where $\mathcal{E}_p$ represents the distance regularization term defined by

$$\mathcal{E}_p(\varphi) = \int_\Omega p\,|\nabla\varphi|\,dx \tag{13}$$

with a potential function p and a constant $\mu > 0$. As suggested in (Li et al., 2010) , we use a double-well function for the potential function p defined by

$$p(s) = \begin{cases} (1-\cos(2\pi s))/4\pi^2 & s \le 1 \\ (s-1)^2/2 & s \ge 1 \end{cases} \tag{14}$$

We have

$$\frac{\partial \mathcal{E}_p}{\partial \varphi} = -\mu \operatorname{div}(D\nabla\varphi) \tag{15}$$

where the diffusion coefficient $D = D(\varphi)$ is given by

$$D(\varphi) = \frac{p'(|\nabla\varphi|)}{|\nabla\varphi|}. \tag{16}$$

We note that p has two minimum points at $s=0$ and $s=1$. It is also twice differentiable with the following properties

$$\left|\frac{p'(s)}{s}\right| < 1 \text{ for } s>0 \text{, and } \lim_{s\to 0}\frac{p'(s)}{s} = \lim_{s\to\infty}\frac{p'(s)}{s} = 1. \tag{17}$$

Given the above properties, one can easily see that

$$\left|\mu\frac{p'(|\nabla\varphi|)}{|\nabla\varphi|}\right| \le \mu. \tag{18}$$

Therefore the diffusion coefficient in (15) will be bounded. Now the new energy functional $\mathcal{F}$ can be minimized by solving the following gradient flow:

$$\begin{aligned} &\frac{\partial\varphi}{\partial t} = \lambda\delta(\varphi)\operatorname{div}\left(g\frac{\nabla\varphi}{|\nabla\varphi|}\right) + \alpha g\delta(\varphi) + \mu\operatorname{div}(D\nabla\varphi) \qquad (x,t)\in\Omega\times[0,\infty) \\ &\varphi(x,0) = \varphi_0(x) \end{aligned} \tag{19}$$

Thanks to the distance regularization term, the central difference scheme can be used to discretize spatial derivatives, which leads to a stable numerical procedure without need of re-initialization (Li et al., 2010).

It also must be noted that, in practice, the functions δ and H are approximated by the smooth functions δ_ε and H_ε defined by (see (Osher and Fedkiw, 2006) and (Zhao et al., 1996))

$$\delta_\varepsilon(x) = \begin{cases} \dfrac{1}{2\varepsilon}\left(1+\cos\left(\dfrac{\pi x}{\varepsilon}\right)\right) & |x| \le \varepsilon, \\ 0 & |x| > \varepsilon; \end{cases} \tag{20}$$

and

$$H_\varepsilon(x) = \begin{cases} \dfrac{1}{2}\left(1+\dfrac{x}{\varepsilon}+\dfrac{1}{\pi}\sin\left(\dfrac{\pi x}{\varepsilon}\right)\right) & |x| \le \varepsilon, \\ 1 & |x| > \varepsilon, \\ 0 & |x| < -\varepsilon; \end{cases} \tag{21}$$

for $\varepsilon > 0$. ε is often considered to be 3/2.

As the boundary condition, we consider the Neumann boundary conditions. For the initial condition, we will consider a simple step function defined by

$$\varphi_0 = \begin{cases} -c_0 & x \in \Omega_0, \\ c_0 & x \in \Omega / \Omega_0; \end{cases} \tag{22}$$

where $c_0 > 0$ is a constant, and Ω_0 is a region inside the image region Ω.

4. Experimental results

We tested our ice layer identification approach on publicly available radar images from 2009 NASA Operation Ice Bridge program. The images were collected with the airborne Multichannel Coherent Radar Depth Sounder system described in (Allen et al., 2012). The images have a resolution of 900 pixels in horizontal direction, which covers around 30km on ground, and 700 pixels in vertical direction, which corresponds to 0 to 4km of ice thickness. For these images there are some ground truth labels that we compared our ice layer identification approach with them. The ground-truth images have been produced by human annotators and some of them are quite noisy and inaccurate and contain only one layer. We chose the images that have both ice and bedrock layers and tested our method on total of 323 images. Since our method is fully automatic we do not need any training dataset and our method is not affected by inaccurate ground-truth. Moreover annotating data by human is quite time consuming and because our method does not need any training and is independent of ground-truthing, it is quite fast. We used the same iteration number of 800 for all of the images.

Figure 3-6 show the results of our approach with respect to the ground-truth. Figure 3a shows the initial curve. This initial curve was drawn automatically; hence there is no need for the user input in any step of the procedure. The entire process is completely automatic. Figure 3b-3e shows the results after iteration 200, 400, 600, and 800respectively. As it can be seen in Figure 3b, after 200 iterations the ice layer is approximately detected but the bedrock is still not detected. After 400 iterations, part of the bedrock is detected, but after 800 iterations both the ice (top layer) and bedrock layers are detected perfectly. Figure 3f shows the ground-truth which is the result of labeling the layers by human. Comparing Figure 3e, the result of the proposed approach, with Figure 3f, the ground-truth, we notice that our result is very close to the ground-truth and is even more accurate in some part. The automated approach proposed in this paper, in addition to being fast and cost effective, increases accuracy in regard to the manual approach. The reason is that in manual procedure experts become tired and careless due to the tediousness of the task.

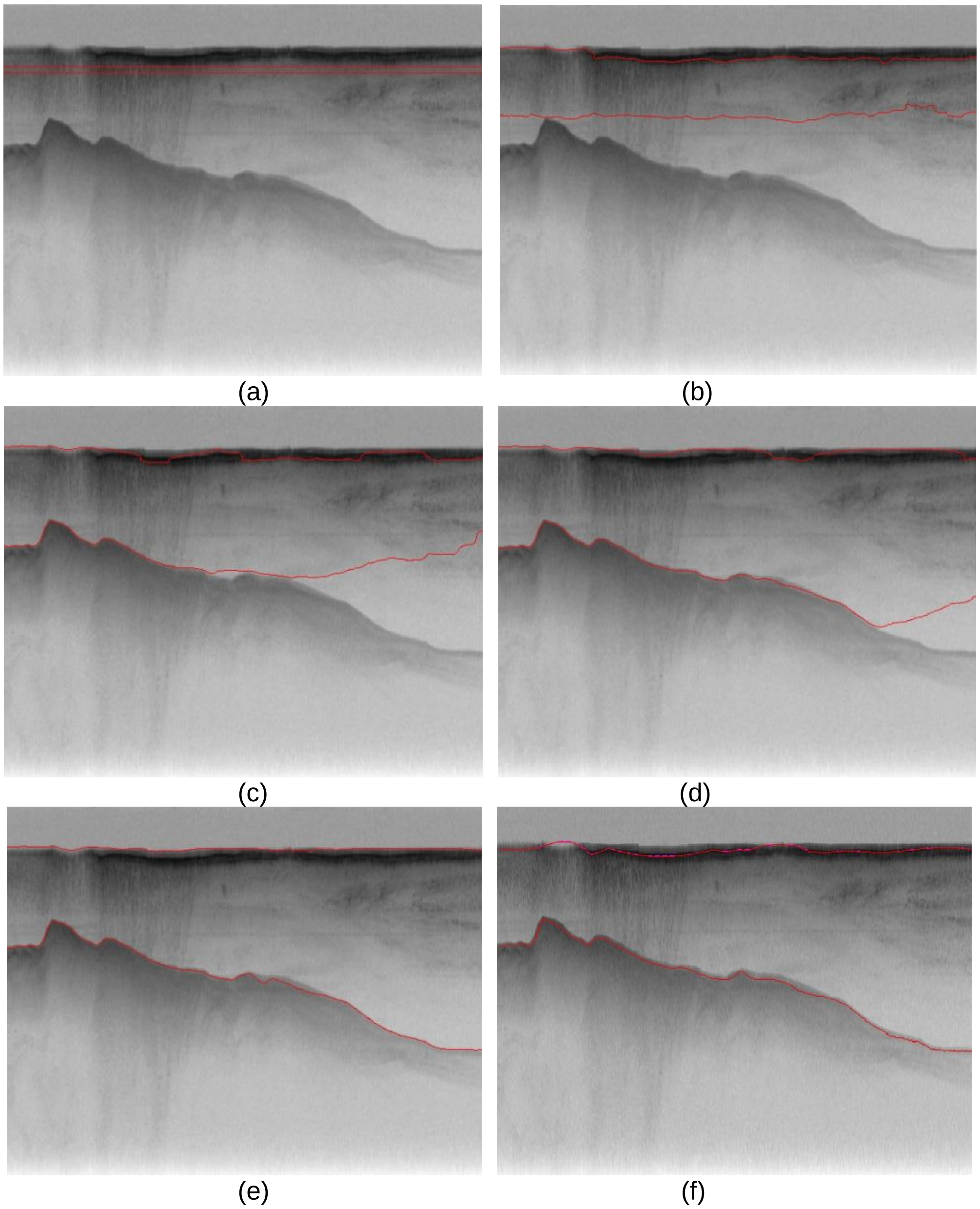

Figure 3: contour evolution throughout processing. a) Initial curve, (b)-(e) contour adaptation to bedrock and ice layer after 200,400,600,800, correspondingly, (f) ground-truth image

Figure 4 shows another example; here the bedrock is rougher with more fluctuation. The same initial curve at previous example was utilized in Figure 4a. After 400 iterations (Figure 4c), the approximate shape of bedrock and ice layers is detected.

After 600 iterations (Figure 4d) the solution is converged and exact shape of both layers are detected. Here we continued the iteration to 800 to have the same conditions for all images. As it can be seen in Figure 4e the perfect shapes of bedrock and ice layers are maintained and extra iterations will not make the situation worse. Comparing our results (Figure 4e) with the ground-truth (Figure 4f), we find our results are more smooth and accurate than ground-truth.

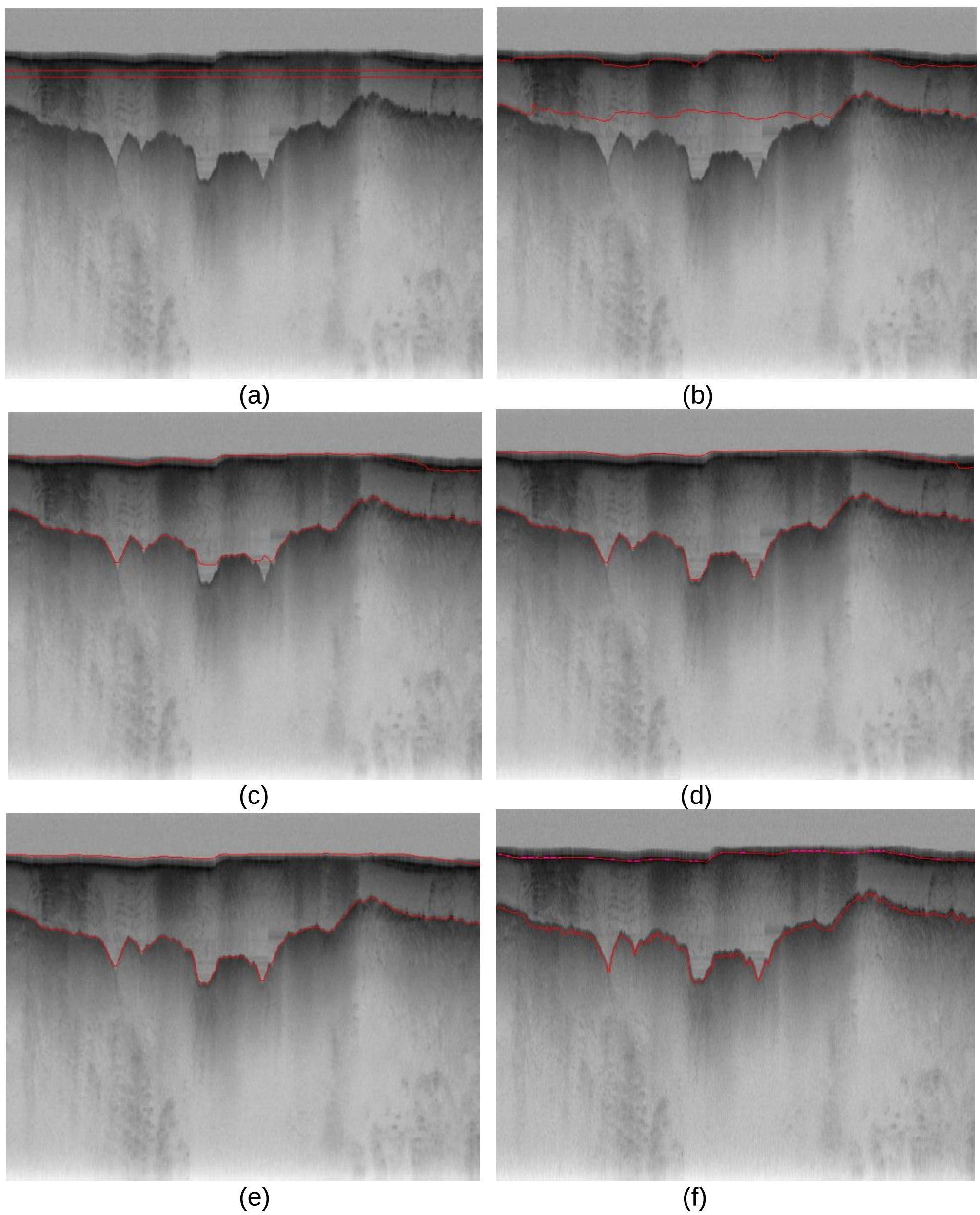

Figure 4: contour evolution throughout processing. a) Initial curve, (b)-(e) contour adaptation to bedrock and ice layer after 200,400,600,800, correspondingly, (f) ground-truth image

Figure 5 demonstrates another example for ice and bedrock layers identification. Here the bedrock is smoother but the image contains more noise especially in the middle layer between ice and bedrock. Here again with the same initial curve and the same number of iterations we got very accurate results comparing to the ground-truth.

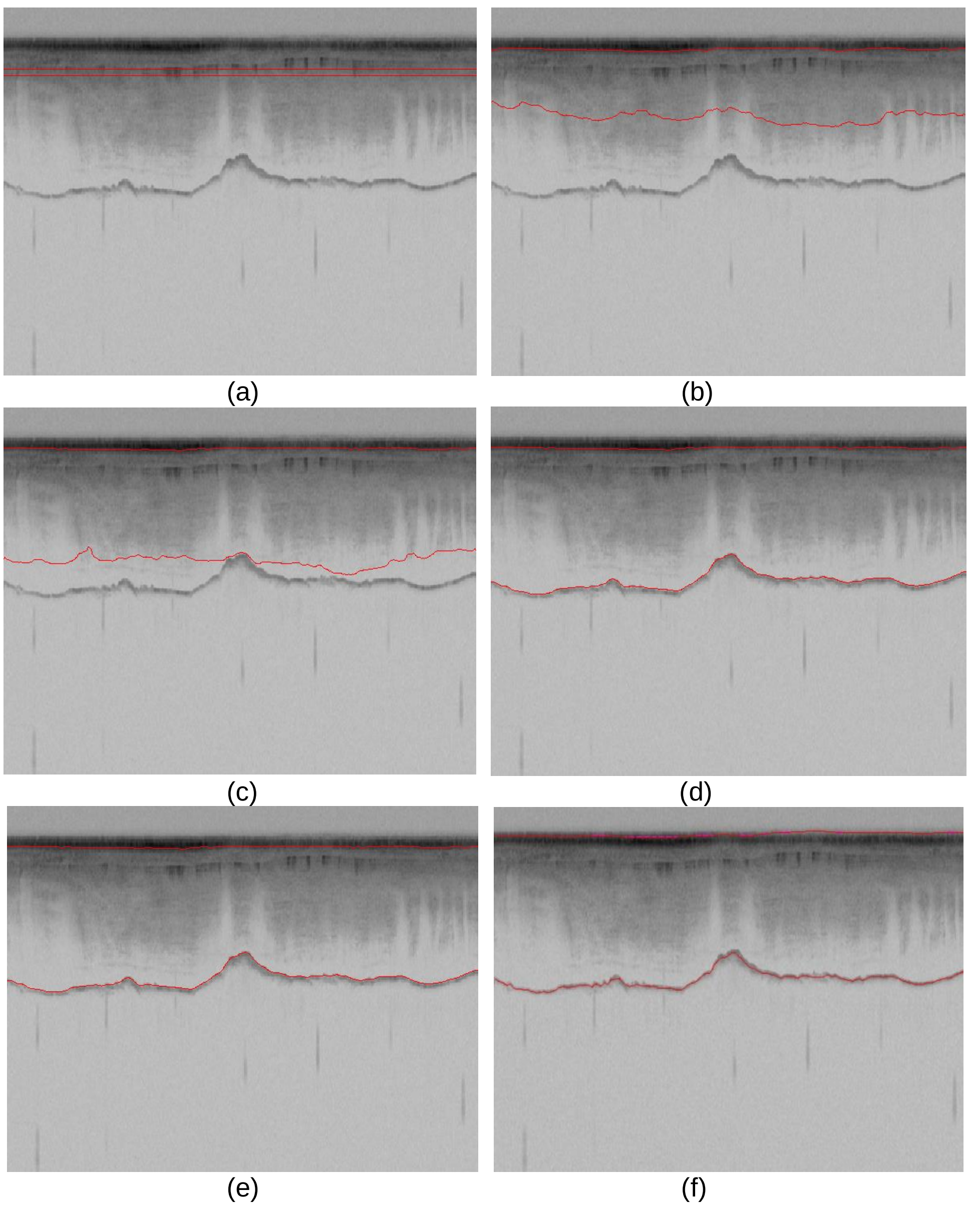

Figure 5: contour evolution throughout processing. a) Initial curve, (b)-(e) contour adaptation to bedrock and ice layer after 200,400,500,800, correspondingly, (f) ground-truth image

Figure 6 is yet another example with more complicated shape of bedrock and with high level of noise in the entire image. Here it takes the entire 800 iterations for the level set solution to converge but it shows a very satisfactory results comparing to the ground-truth.

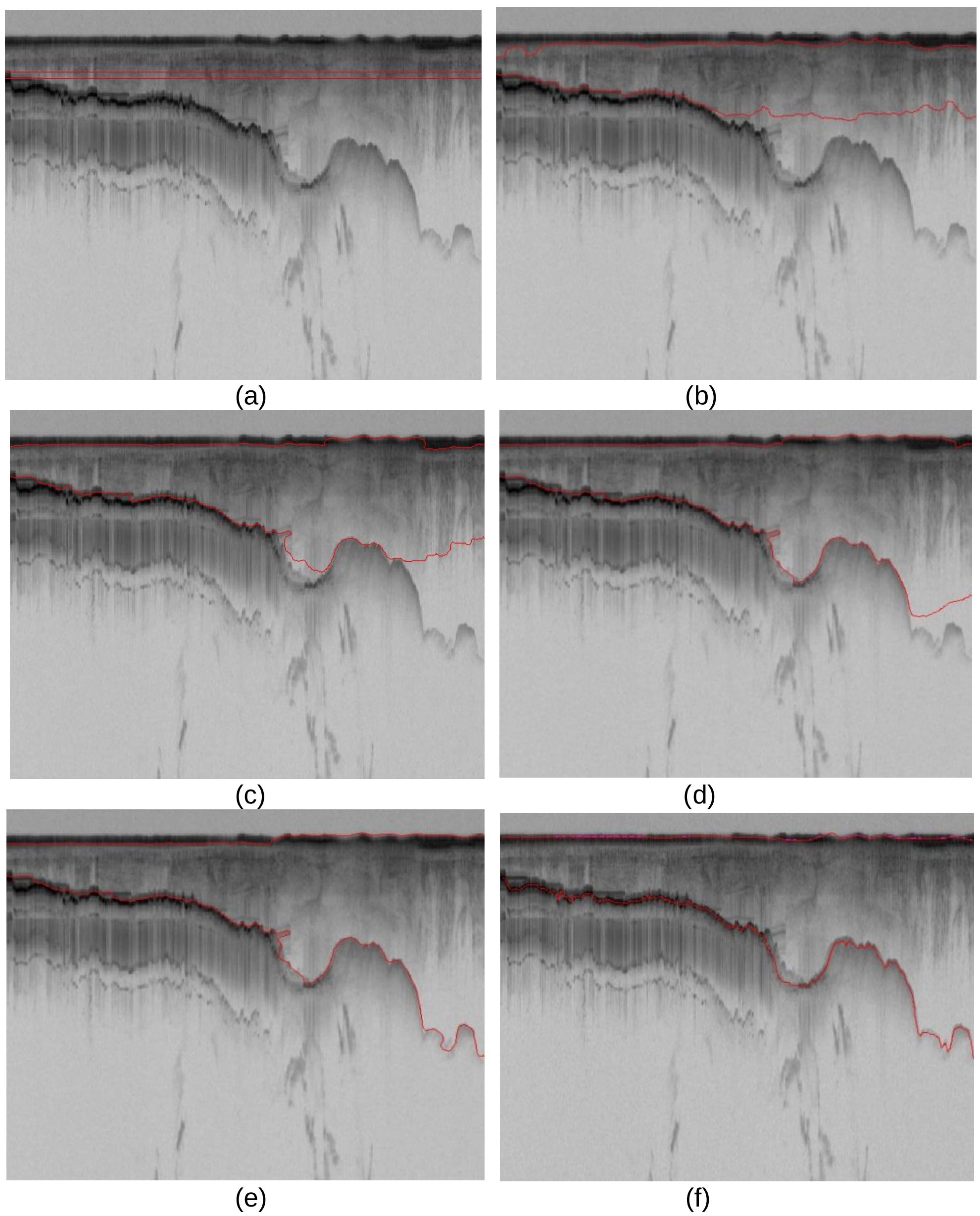

Figure 6: contour evolution throughout processing. a) Initial curve, (b)-(e) contour adaptation to bedrock and ice layer after 200,400,600,800, correspondingly, (f) ground-truth image

Figure 7 shows some of the representative results for the ice and bedrock layer identification for various shapes of bedrock from a very smooth bedrock to a rough and very oscillating bedrock with different levels of noise. In all of the examples, the results with the automatic level-set approach (the left column) is as accurate as ground-truth (the right column). However in the last two rows (f1 and g1) due to high level of fluctuations in the bedrock, still after 800 iterations it could not detect all parts of the bedrock. However the results are very close to ground-truth and more iteration will create more accurate results. In this study we used the constant iterations of 800 for all of the images in the dataset.

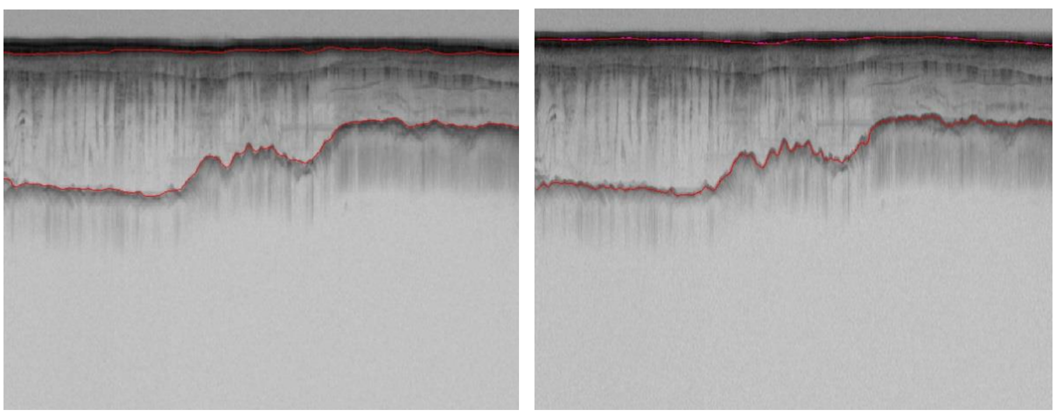

(a1) (a2)

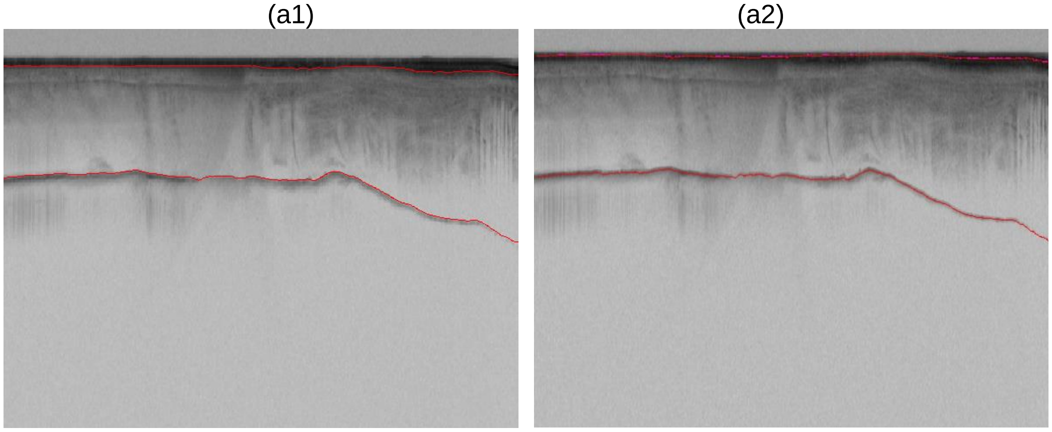

(b1) (b2)

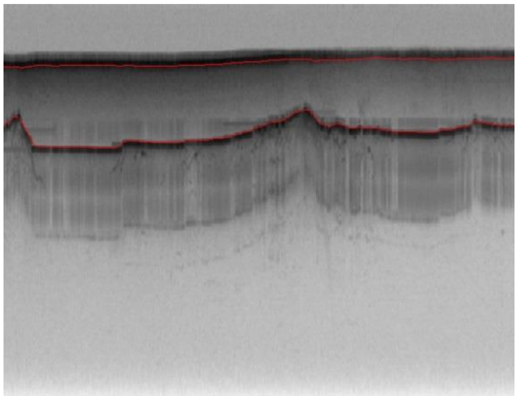
(c1)

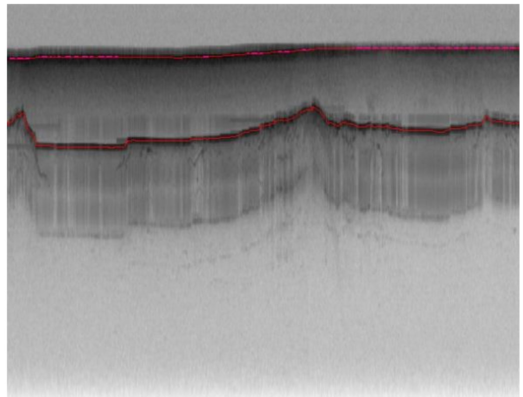
(c2)

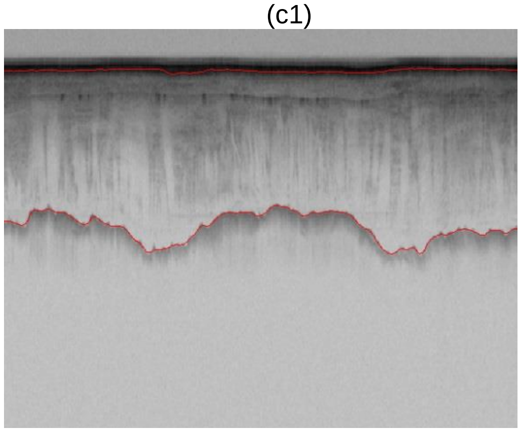
(d1)

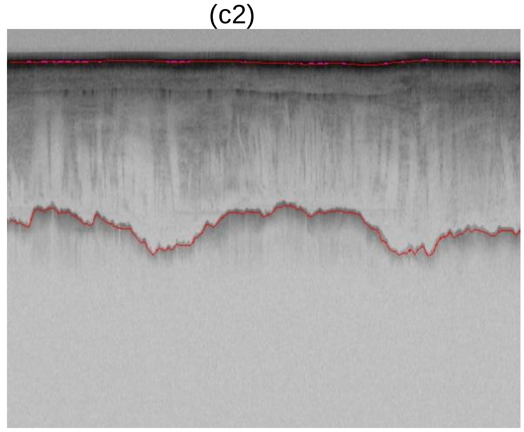
(d2)

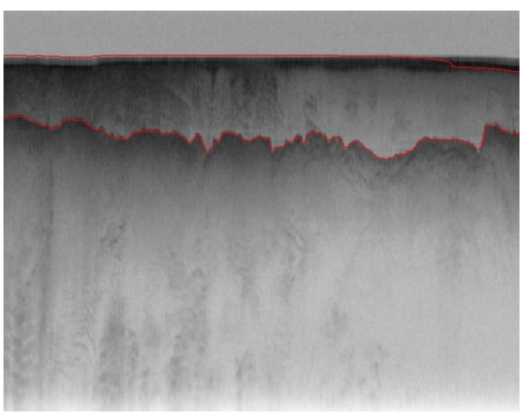
(e1)

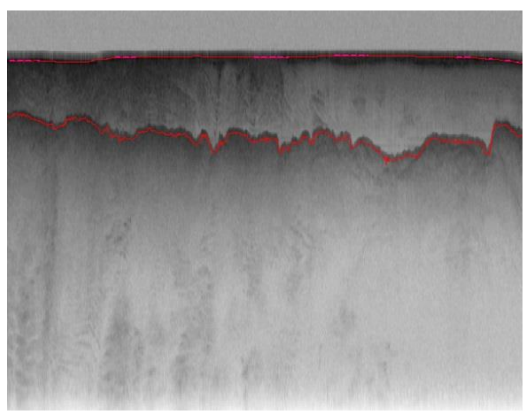
(e2)

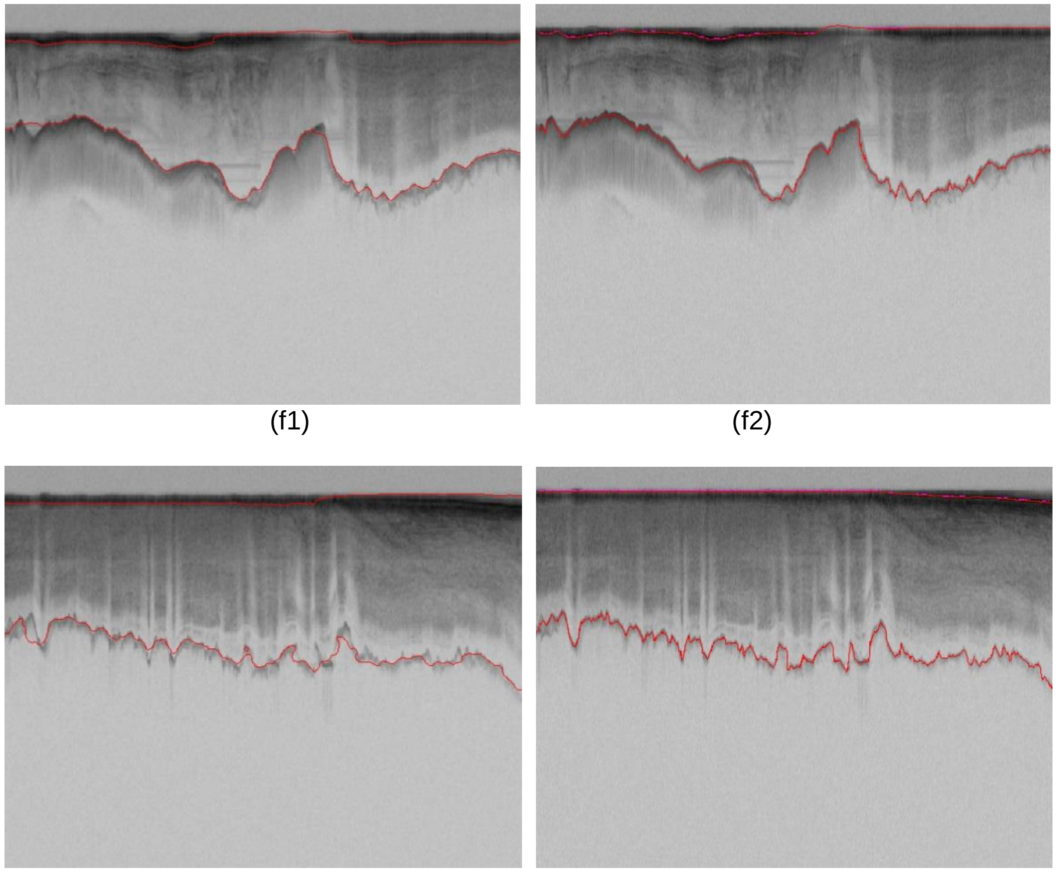

(f1) (f2)

(g1) (g2)

Figure7: Bedrock and ice layer detection by proposed method, left column: the result of the proposed level set approach, Right column: ground-truth

5. Evaluation

To evaluate the performance of our proposed method first we need to set up some benchmarks. For any particular piece of data that we are evaluating there are four states. Whether it is correctly belonging to a class or not belonging to a class. This information is normally displayed in a confusion matrix (Table 1).

Table 1: Confusion Matrix

	Actual Class (Observation)	
Predicted Class (Expectation)	TP (True Positive) Correct result	FP (False Positive) Unexpected result
	FN (False Negative) Missing result	TN (True Negative) Correct absence of result

In the confusion matrix, TP is true positive or correct result, FP is false positive or unexpected result, FN is false negative or missing results, and TN is true negative or correct absence of results. From the confusion matrix recall (R) and precision (P) are calculated as follow:

$$R = \frac{TP}{TP + FN} \tag{23}$$

$$P = \frac{TP}{TP + FP} \tag{24}$$

Precision measures the exactness of a classifier while recall measures the completeness or sensitivity of a classifier. Precision and recall can be combined to produce a single metric known as *F-measure*, which is the weighted harmonic mean of precision and recall. The F-measure defined as:

$$F = \frac{1}{\alpha \frac{1}{p} + (1-\alpha)\frac{1}{R}} = \frac{\left(\beta^2 + 1\right)PR}{\beta^2 P + R} \tag{25}$$

captures the precision and recall tradeoff. The F-measure is valued between 0 and 1, where larger values are more desirable. In this paper we used balanced F-measure, i.e. with $\beta = 1$.

The assumption is that human labeled images (ground-truth) contain perfect results and then the performance of our method was evaluated with respect to ground-truth. We calculated the precision, recall and F-measure for 323 images. Figure 8 shows F-measure for all of the images. In our dataset around 65% of the images have invisible or faint bedrock layers. For the images that bedrock is not completely visible in the image (Figure 9) our approach is not able to detect the invisible part accurately. For these images it is better to stop the iteration early otherwise its error will be accumulated. However to avoid human interference we kept the iteration of 800 for all of the images and reached 75% accuracy for the entire dataset. For the images that have visible bedrock layers (1/3 of dataset), we reached the average accuracy of 96% (Table 2). Our algorithm is very fast, taking an average of 30 second to process each image on a 2.7 GHz machine. Moreover it does not need any training phase with human labeled images which speed up the entire process significantly. Usually it takes up to 45 minutes per file to manually label the image (Gifford et al., 2010).

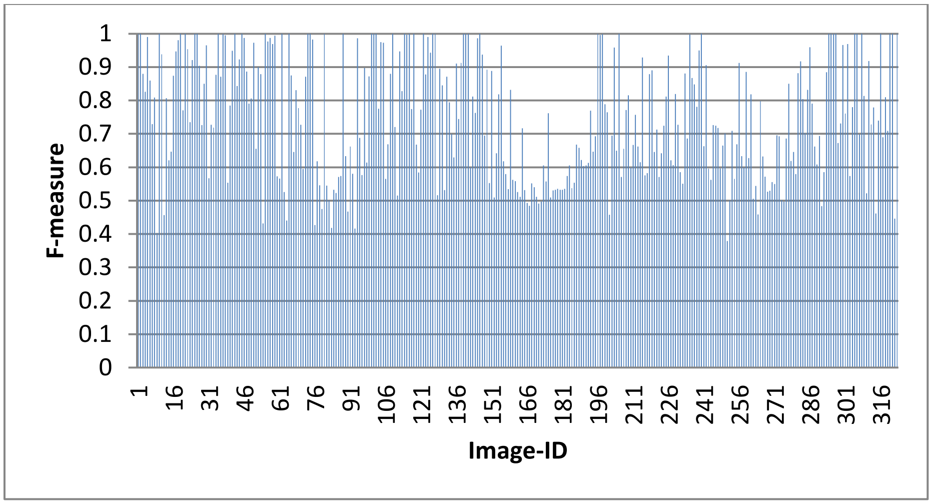

Figure 8: F-measure for 323 images

Table 2: Average F-measure of our approach for the entire dataset and also for the images with visible bedrocks

	F-measure
Entire dataset (visible and invisible bedrock layers)	75%
Images with visible bedrock	96%

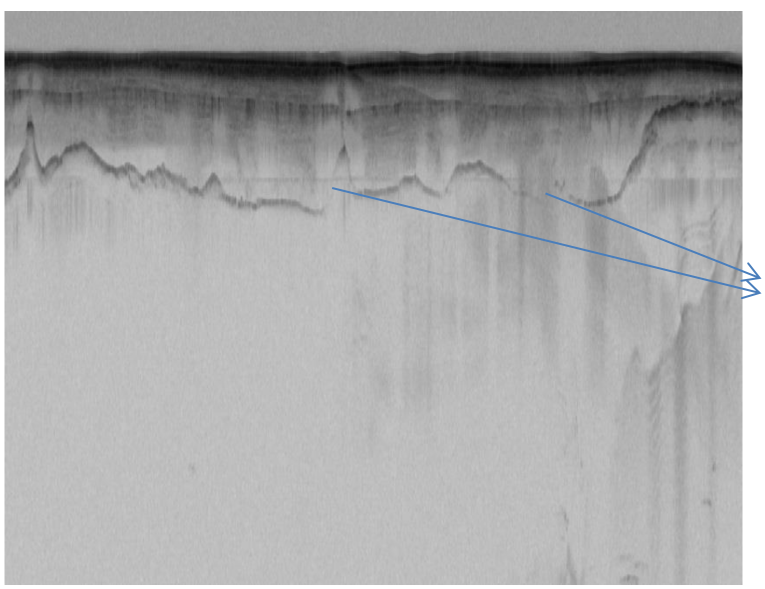

(a)

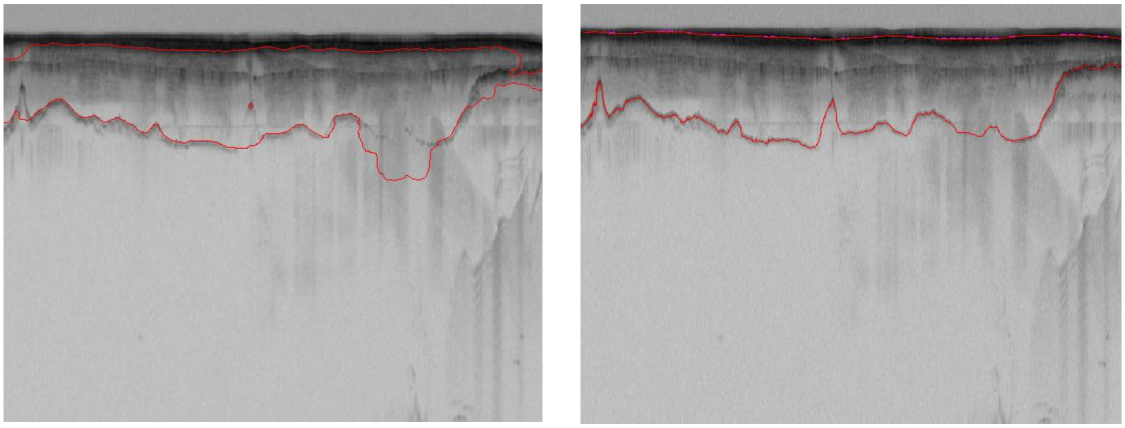

(b) (c)

Figure 9: our approach is not able to detect the invsible parts of bedrock, a) original image, b) the icelayer and bedrock detected by our approach, c) ground-truth

6. Conclusion

We presented an automatic approach to estimate bedrock and ice layers in multichannel coherent radar imagery. In this approach the complex topology of ice and bedrock boundary layers were detected by evolving an initial curve in radar imagery. The results were evaluated on a large dataset of airborne radar imagery collected during IceBridge mission over Antarctica and Greenland and show promising results in respect to hand-labeled ground truth. We reached the high accuracy of 75% for the entire dataset using a fully automatic technique. Some images present faint or invisible bedrock layers and are nearly impossible to automatically detect them with 100% accuracy. For those images it is better to first separate them from the images that have visible bedrock layer. In future we are planning to extend this work by improving the quality of the image in invisible areas in bedrock prior to applying level set algorithm.

7. References

Allen, C., Shi, L., Hale, R., Leuschen, C., Paden, J., Pazer, B., Arnold, E., Blake, W., Rodriguez-Morales, F., Ledford, J. (2012) Antarctic ice depthsounding radar instrumentation for the NASA DC-8. Aerospace and Electronic Systems Magazine, IEEE 27, 4-20.

Chan, T.F., Vese, L. (2001) Active contours without edges. Image Processing, IEEE Transactions on 10, 266-277.

Crandall, D.J., Fox, G.C., Paden, J.D., (2012) Layer-finding in Radar Echograms using Probabilistic Graphical Models, Pattern Recognition (ICPR), 21st International Conference on.

Fahnestock, M., Abdalati, W., Luo, S., Gogineni, S. (2001) Internal layer tracing and age-depth-accumulation relationships for the northern Greenland ice sheet. Journal of Geophysical Research: Atmospheres (1984–2012) 106, 33789-33797.

Ferro, A., Bruzzone, L., (2011) A novel approach to the automatic detection of subsurface features in planetary radar sounder signals, Geoscience and Remote Sensing Symposium (IGARSS), 2011 IEEE International. IEEE, pp. 1071-1074.

Freeman, G.J., Bovik, A.C., Holt, J.W., (2010) Automated detection of near surface Martian ice layers in orbital radar data, Image Analysis & Interpretation (SSIAI), 2010 IEEE Southwest Symposium on. IEEE, pp. 117-120.

Frigui, H., Ho, K., Gader, P. (1900) Real-time landmine detection with ground-penetrating radar using discriminative and adaptive hidden Markov models. EURASIP Journal on Advances in Signal Processing 2005, 1867-1885.

Gifford, C.M., Finyom, G., Jefferson Jr, M., Reid, M., Akers, E.L., Agah, A. (2010) Automated polar ice thickness estimation from radar imagery. Image Processing, IEEE Transactions on 19, 2456-2469.

Ilisei, A.-M., Ferro, A., Bruzzone, L., (2012) A technique for the automatic estimation of ice thickness and bedrock properties from radar sounder data acquired at Antarctica, Geoscience and Remote Sensing Symposium (IGARSS), 2012 IEEE International. IEEE, pp. 4457-4460.

Karlsson, N.B., Dahl-Jensen, D., Gogineni, S.P., Paden, J.D. (2013) Tracing the depth of the Holocene ice in North Greenland from radio-echo sounding data. Annals of Glaciology 54, 44-50.

Kass, M., Witkin, A., Terzopoulos, D. (1988) Snakes: Active contour models. International journal of computer vision 1, 321-331.

Lee, S.-R., Mitchell, J., Crandall, D.J., Fox, G.C., (2014) Estimating bedrock and surface layer boundaries and confidence intervals in ice sheet radar imagery using MCMC, Image Processing (ICIP), 2014 IEEE International Conference on. IEEE, pp. 111-115.

Li, C., Xu, C., Gui, C., Fox, M.D., (2005) Level set evolution without re-initialization: a new variational formulation, Computer Vision and Pattern Recognition, 2005. CVPR 2005. IEEE Computer Society Conference on. IEEE, pp. 430-436.

Li, C., Xu, C., Gui, C., Fox, M.D. (2010) Distance regularized level set evolution and its application to image segmentation. Image Processing, IEEE Transactions on 19, 3243-3254.

Mitchell, J.E., Crandall, D.J., Fox, G., Paden, J., (2013a) A semi-automatic approach for estimating near surface internal layers from snow radar imagery, IGARSS, pp. 4110-4113.

Mitchell, J.E., Crandall, D.J., Fox, G.C., Rahnemoonfar, M., Paden, J.D., (2013b) A semi-automatic approach for estimating bedrock and surface layers from multichannel coherent radar depth sounder imagery, SPIE Remote Sensing. International Society for Optics and Photonics, pp. 88921E-88921E-88926.

Osher, S., Fedkiw, R. (2006) Level set methods and dynamic implicit surfaces. Springer Science & Business Media.

Osher, S., Sethian, J.A. (1988) Fronts propagating with curvature-dependent speed: algorithms based on Hamilton-Jacobi formulations. Journal of computational physics 79, 12-49.

Sime, L.C., Hindmarsh, R.C., Corr, H. (2011) Instruments and methods automated processing to derive dip angles of englacial radar reflectors in ice sheets. Journal of Glaciology 57, 260-266.

Zhao, H.-K., Chan, T., Merriman, B., Osher, S. (1996) A variational level set approach to multiphase motion. Journal of computational physics 127, 179-195.